Facile preparation of mesoporous TiO$_2$(B) nanowires with well-dispersed Fe$_2$O$_3$ nanoparticles and their photochemical catalytic behavior

Lei Qin [a], Xiaoxue Pan [a], Ling Wang [a,b], Xiping Sun [a], Guoliang Zhang [a,*], Xinwen Guo [c]

[a] Center for Membrane and Water Science, College of Chemical Engineering and Material Science, Zhejiang University of Technology, Hangzhou 310014, China
[b] Hangzhou Special Equipment Inspection and Research Institute, Hangzhou 310003, China
[c] State Key Laboratory of Fine Chemicals, Department of Catalysis Chemistry and Engineering, Dalian University of Technology, Dalian 116012, China

ARTICLE INFO

ABSTRACT

We report a facile impregnation–solvothermal method for the preparation of mesoporous TiO$_2$(B) nanowires (TNWs(B)) supporting with Fe$_2$O$_3$ nanoparticles (NPs). Open tunnel and porous structure of TNWs(B) provided a confined micro-environment for the stabilization of well-dispersed nanoparticles. The intact fibrous morphology structure, high crystallinity and porosity were remained for TNWs(B) after supporting by nanoparticles. UV−visible DRS analysis indicated that the loading of Fe$_2$O$_3$ on TNWs(B) promoted light harvesting ability and further extended the absorption range. The photocatalytic experiments showed that Fe$_2$O$_3$/TNWs(B) had remarkable catalytic activity for photochemical oxidation of organic pollutants Direct Red 4BS in presence of H$_2$O$_2$ and exhibited excellent tolerance with respect to organic matter poisoning, which was attributed to favorable synergetic effect of Fe$_2$O$_3$ NPs and TNWs(B) support. Compared with P25, the composite material taking the advantage of fibrous morphology was more easily separated from reaction system simply by sedimentation. Moreover, the greatest interest of our finding would be exploring that impregnation duration had significant effect on size and location of NPs supported on TNWs(B). When impregnation duration time was higher than 12 h, NPs with $d < 2$ nm were highly dispersed in porous nanoarchitecture and had positive effect on catalytic performance, which was due to the facilitation of interfacial photo-generated electrons transfer between (0 0 1) planes in TiO$_2$(B) and (1 1 3) planes of Fe$_2$O$_3$. The high-degree control over size and location of nanoparticles provides valuable insights for understanding relationship between structure and catalytic activity.

© 2014 Elsevier B.V. All rights reserved.

1. Introduction

TiO$_2$ materials are of great practical importance due to its high photoreactivity, nontoxicity, stability, and low cost [1–5]. Besides three well-known crystallographic forms of anatase (tetragonal), rutile (tetragonal), and brookite (orthorhombic), TiO$_2$(B), as a metastable monoclinic modification of TiO$_2$ with a crystal structure, was first discovered in 1980 [6]. The structure of TiO$_2$(B) crystal consists of two edge-sharing octahedra linked to the neighboring doublet octahedra unit at their corners. Recently, TiO$_2$(B) materials have been a topic of much interest due to their open tunnel structure, significant voids and abundant surface states or oxygen vacancies, and lower density than that of anatase [7]. Among various nano architectures of TiO$_2$(B) materials, immense efforts are devoted to the study of one-dimensional (1D) nanostructures such as nanowires, nanotubes, nanobelts, and nanofibers due to their unique physical and chemical properties and tremendous advantages of rapid, diffusion-free electron transport along the longest direction over commonly used nanoparticles (NPs) [8–10], which have been intensively investigated in Li-ion batteries [11,12], dye sensitized solar cells [13], photocatalysis [14], and catalyst supports [15].

However, in view of photocatalytic applications, the lower catalytic activity of TiO$_2$(B) materials than anatase TiO$_2$ is still a major obstacle for achieving superior quality [16,17]. If its photocatalytic activity can be improved by a certain surface modification, the

TiO_2(B) nanostructures would guide us toward a highly promising alternative for the present photocatalysis. To solve this problem, many efforts have been devoted to develop different strategies to enhance the activity of TiO_2(B) materials. So far, most of previous researches were focused on designing core–shell nanoparticles of the anatase–TiO_2(B) mixed phase to improve its photocatalytic activity by means of a difference in the conduction band edge of the two phases [18,19]. In comparison, another effective strategy was to construct TiO_2(B) hybrid nanostructure with highly additional nanophase such as metal NPs (Au and Pt) [20,21]. Because the metals or even metal oxides with suitable band gaps can improve the photo-stimulated charge separation and suppress charge recombination of TiO_2, the photocatalytic efficiency will be enhanced [22–24]. Among them, Fe_2O_3 NPs, as an interesting n-type semiconducting material, are not only abundant, cheap and with narrow band gap (about 2.2 eV), but also can promote the interface charge transfer of heterostructured materials, which is considered as a great alternative to be supported to enhance photocatalytic activity [25]. Some researchers prepared TiO_2 nanotube arrays functionalized by Fe_2O_3 nanoparticles, which presented excellent photocatalytic activity for degradation of organic contaminants [26–28]. However, little work has yet been reported on enhancing the photocatalytic activity of TiO_2(B) nanomaterials by loading of the metal oxide nanoparticles.

We herein report our progresses on the preparation of mesoporous TiO_2(B) nanowires (TNWs(B)) with well dispersed Fe_2O_3 nanoparticles as efficient catalysts via a simple impregnation–solvothermal method for the first time. TNWs(B), as a superior host, can provide a confined micro-environment for the stabilization of highly dispersed metal or metal oxide nanoparticles and be separated readily from photocatalytic reaction mixture to be reused due to the fibrous morphology, discontinuous lattice fringes, and mesoporous structure [29,30]. Importantly, 1D long nanowires, as raw materials, can also be used for direct fabrication of multifunctional paper-like free standing membrane and self-assembly microsphere. TiO_2 nanowire membrane has the distinctive mesh structure and can provide concurrent separation and photocatalytic degradation for the water purification, while TiO_2 nanowire basketry-like microspheres can exhibit macroporous channels in spheres structure, and serve as light-transfer paths for the distribution of photo energy to improve the photoactivity [31–33].

In this context, our attempts have also been made to characterize the microscopic properties of the dispersion and location of metal oxides immobilized on the surface of TNWs(B). The effects of impregnation duration time on the size and location of Fe_2O_3 nanoparticles supported on the TNWs(B) were investigated, and the size–activity relationship in the hybrid materials was deduced. We hope that the method described in this paper will provide a new and effective route to the rational design of highly active TNWs(B) composite materials. More importantly, we try to propose a new opinion for enhancing the decomposition of H_2O_2 to hydroxyl radical by the favorable synergetic effect between the metal oxides NPs and the support.

2. Experimental

2.1. Chemicals

The commercial dye Direct Red 4BS was available from Betapharma (Shanghai, China) and used without further purification. All chemicals, such as hydrogen peroxide (H_2O_2, 30%, w/w), $Fe(NO_3)_3 \cdot 9H_2O$, $CuSO_4$, HCl, and NaOH, were of analytical grade and were purchased from Sinopharm chemical Reagent Co., China. All experiment solutions were prepared from deionized water manufactured by a self-made RO–EDI system, in which ion concentration was analyzed by IRIS Intrepid ICP and Metrohm 861

Compact IC and controlled to meet the requirement of conductivity $\sigma \le 0.5\,\mu S\,cm^{-1}$.

2.2. Synthesis of TiO_2(B) nanowires support

In a typical synthesis of TiO_2(B) nanowires, 1.5 g of TiO_2 powers (Aeroxide® P25, Evonik) were introduced into 140 mL of 10 M NaOH solution in a 200 mL Teflon-lined autoclave container. After hydrothermal reaction on an oven for 48 h at 473 K, the white pulp-like product of nanowires were collected, washed with deionized water and dilute HCl, and then dried at 353 K for 8 h. The resulting samples were then calcined at 673 K for 4 h.

2.3. Preparation of Fe_2O_3/TiO_2(B) nanowires composite

The loading of TiO_2(B) nanowires with Fe_2O_3 nanoparticles were performed by an impregnating–solvothermal method. The 0.55 g as-prepared TNWs(B) were dispersed in an 80 mL of ethanol/water mixture (1:1, v/v) containing the Fe^{3+} ions (5% TNWs(B), w/w %). The mixture was stirred at room temperature to form a homogeneous solution, and then transformed into the Teflon-lined autoclave container and held at 353 K for 8 h. Finally, the obtained yellow powders were washed with distilled water and dried under vacuum condition. By applying this procedure, four composite materials with different stirring time of 0 h, 6 h, 12 h and 18 h were obtained and abbreviated as $Fe_2O_3/TNWs$(B)-0, $Fe_2O_3/TNWs$(B)-6, $Fe_2O_3/TNWs$(B)-12 and $Fe_2O_3/TNWs$(B)-18, respectively.

2.4. Characterization

The morphology of the prepared samples was evaluated using Hitachi JEM-1200EX transmission electron microscopy (Hitachi, Tokyo, Japan) and Tecnai G2 F30 S-Twin high resolution transmission electron microscopy (Philips-FEI, Holland). Energy dispersive spectroscopy (Hitachi, S-3700N, Tokyo, Japan) was also taken for the composition analysis of the samples. The X-ray diffraction (XRD) patterns of the samples were determined by using X'Pert PRO X-ray diffractometer (PNAlytical, Cu $K\alpha$ radiation), in which the accelerating voltage and emission current were 40 kV and 100 mA, respectively. Raman spectra of the samples were obtained on a HORIBA OLYMPAS BX41 with excitation wavelength of 532 nm. Surface properties of the samples were examined by X-ray photoelectron spectroscopy (XPS). XPS experiments were carried out on a RAD upgraded PHI-5000C ESCA system (Perkin-Elmer) with Mg $K\alpha$ radiation ($h\nu$ = 1253.6 eV) and binding energies were calibrated by using at 10.0 kV and 20.0 mA, respectively. All the binding energies were referenced to the C1s peak at 284.6 eV. Nitrogen adsorption−desorption isotherms and specific surface areas were obtained at 77 K using an ASAP 2020 surface area and porosity analyzer (Micromeritics, USA), and their pore size distributions were determined by the BJH (Barrett–Joyner–Halenda) method. The light adsorption properties of the prepared catalysts were examined by measuring their UV/visible diffuse reflectance spectra, which were performed on a Varian Cary 500 Scan UV–visible spectrometer (Varian, USA) with $BaSO_4$ as the reflectance standard. The compositional analysis of catalysts was performed by ICP in an Optima 2000 instrument (PerkinElmer, USA) after the samples microwave digestion in HNO_3/H_2SO_4 solution.

2.5. Catalytic experiments

The catalytic experiment was carried out in a glass cylinder in a 1 L glass batch reactor under vigorous stirring at around 298 K. The irradiation was performed with a 150 W UV–visible lamp and the lamp was surrounded by a tube in which a copper sulphate aqueous solution was used to cut off radiation with a wavelength

shorter than 310 nm. Appropriate amounts of the samples were suspended in 750 mL of Direct Red 4BS solution. The suspension was stirred continuously in darkness for 30 min to ensure the equilibrium adsorption of 4BS by the catalyst. The pH of the reaction mixture was adjusted by using HCl and NaOH solutions. A certain content of H_2O_2 was added to the mixture, and then the lamp was switched on to initiate the reaction. The concentration of dye in samples was measured by U-2910 digital spectrophotometer
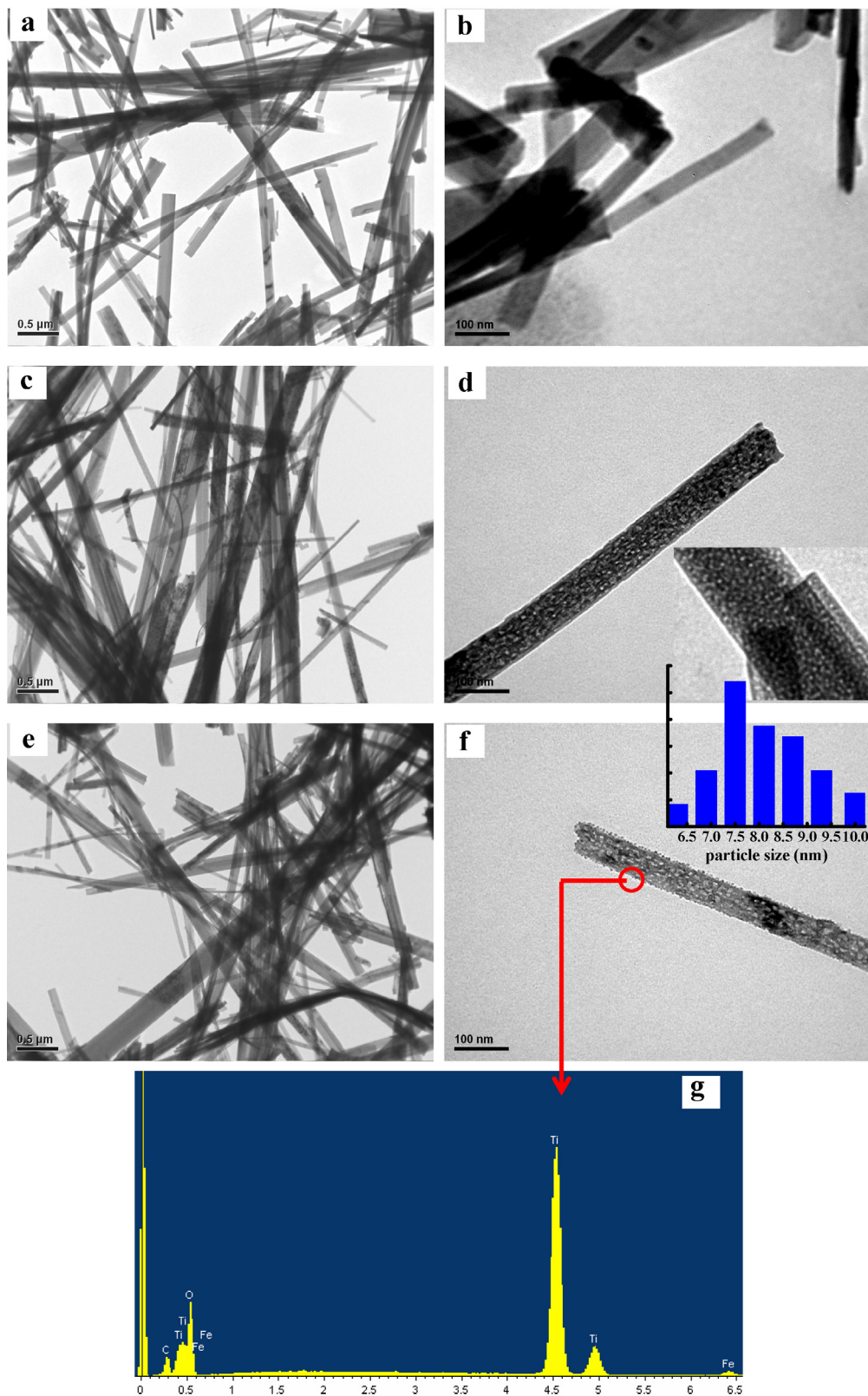

Fig. 1. TEM images of TiO_2 nanowires precursor (a, b), pure TNWs(B) (c, d), and Fe_2O_3/TNWs(B) (e, f); and EDX spectrum of Fe_2O_3/TNWs(B) (g). The inset of (f) is the size distribution of metal oxide nanoparticles corresponding to the catalyst.

(Hitachi, Japan) filtered directly through a 0.45 μm microfiltration membrane. Iron contents in the filtered solution after reaction was determined by 55B type AAS (Varian, USA) equipped hollow cathode Fe lamp (sensitive line, 248.3 nm; slits, 0.4 nm; operating current, 4 mA).

3. Results and discussion

3.1. Morphology and structure of TiO$_2$(B) nanowires and Fe$_2$O$_3$/TiO$_2$(B) nanowires

The typical TEM images of TiO$_2$ materials are shown in Fig. 1. It presents uniform 1D nanowire-like structure and highly oriented growth behavior after hydrothermal treatment (Fig. 1a and b). TiO$_2$ nanowires are of typical width 50–200 nm and can extend up to 1–10 μm in length. In order to obtain TiO$_2$(B) phase, the TiO$_2$ nanowires precursor needs to be annealed in air atmosphere at 673 K for 4 h. As illustrated by TEM images (Fig. 1c and d), it can be found that the morphology of the TNWs(B) did not change after heat treatment, but a highly porous texture clearly appeared as the white dot-like objects outside the surface. Fig. 1e and f displays the detailed morphological information of the Fe$_2$O$_3$/TNWs(B) composite. As shown in Fig. 1e, the hybrid materials have a linear morphology with the same particle size as the bare TiO$_2$ nanowires after decorated with Fe$_2$O$_3$. By careful comparison, the mesoporous network of the nanowires surface can still be clearly observed (Fig. 1f), which is similar to the bare TiO$_2$(B) nanowires. This indicates that the crystalline order of the TNWs(B) host remains intact after loading. Importantly, TEM images give an obvious evidence for metal oxide NPs which are distributed over the out surface and pore of TNWs(B) matrix in a homogeneous fashion with a size varied from 6.0 to 10.0 nm (the inset of Fig. 1f). Fig. 1g shows the EDX pattern of the supported nanowires, which reveals the presence of the Fe, Ti, and O elements. No impurities were observed in the samples.

The crystalline structures of nanowires are presented in Fig. 2a. In the diffraction pattern of TiO$_2$ nanowires precursor, 2θ of 10.66°, 24.83°, 29.26°, and 48.63° are reflections from the (2 0 0) planes of H$_2$Ti$_5$O$_{11}$·H$_2$O (JCPDS 44-0131) and the (2 0 2), (3 1 0), and (1 1 4) planes of H$_2$Ti$_3$O$_7$ (JCPDS 47-0561), respectively. This indicates that the prepared nanowires possessed a mixed phase structure. After calcinated at 673 K, the H$_2$Ti$_5$O$_{11}$·H$_2$O and H$_2$Ti$_3$O$_7$ nanowire core is converted into TiO$_2$(B) single crystal. Five distinct well-resolved characteristic diffraction peaks of TiO$_2$ nanowires corresponds to the TiO$_2$(B) phase (JCPDS 46-1237). When supporting by iron oxide, the diffraction peaks associated with the nanowires are somewhat broadened and shifting slightly to the higher diffraction angles, while the TiO$_2$(B) crystals in the composite remains unchanged. These changes were mainly attributed to the crystallographic defect since the substitution of Ti^{4+} by Fe^{3+} ions [34]. However, it does not provide any indication of iron oxide crystalline phases in diffraction pattern of Fe$_2$O$_3$/TNWs(B), which deduces that the loading of NPs could be well dispersed in the TiO$_2$ nanowires structure.

Fig. 2b shows the Raman spectra of TNWs(B) and Fe$_2$O$_3$/TNWs(B). Raman spectroscopy of prepared TiO$_2$ nanowires further confirms that it is assigned to the structure of typical TiO$_2$(B) nanomaterials [10,35]. While the nanoparticles supported on TiO$_2$ nanowires show a similar Raman bands, no obvious Raman bands of Fe$_2$O$_3$ are confirmed. However, it should be noted that the incorporation of metal oxides nanoparticles leads to characteristic peak intensities decreasing dramatically and shifting slightly to the higher frequency as evidenced by the position of the main peak in Raman spectra. This may be due to the fact that the Fe atoms incorporated to the lattice of support causes the distortion
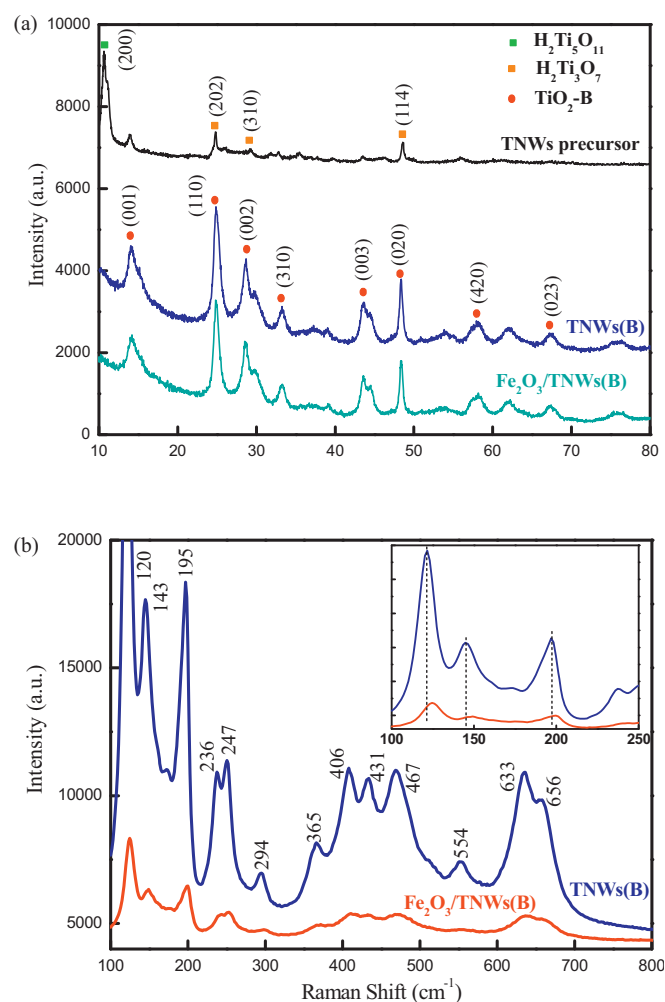

Fig. 2. XRD patterns (a) and Raman spectra (b) of different prepared catalysts.

of crystalline lattice and surface iron oxides shield visible light for excitation of TiO$_2$.

The nitrogen adsorption/desorption isotherms and pore size distribution curve were investigated to evaluate the surface area and pore size distribution of the TNWs(B) and Fe$_2$O$_3$/TNWs(B). As seen in Fig. 3, the isotherms of both TNWs(B) and Fe$_2$O$_3$/TNWs(B) show a typical IV type pattern with a hysteresis loop in the low relative (P/P_0) range of 0.3–0.8, which indicates the occurrence
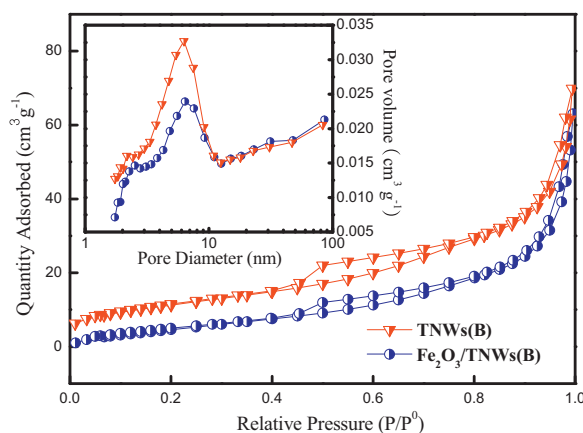

Fig. 3. Adsorption/desorption isotherms and BJH pore size distribution for pure TNWs(B) and Fe$_2$O$_3$/TNWs(B).

Table 1
Surface area and textural data for synthesized different samples.

Sample	S_{BET} (m^2 g^{-1})[a]	$S_{Langmuir}$ (m^2 g^{-1})[b]	S_{BJH} (m^2 g^{-1})[c]	V_{meso} (cm^3 g^{-1})[d]	Average pore diameter (nm)[e]
TNWs(B)	41.23	66.83	51.15	0.109	9.50
Fe$_2$O$_3$/TNWs(B)	34.42	54.94	37.08	0.107	11.42

[a] S_{BET} is the BET specific surface area.
[b] $S_{Langmuir}$ is the Langmuir specific surface area.
[c] S_{BJH} is the BJH adsorption cumulative surface area of pores of 1.70–300.00 nm in diameter.
[d] V_{meso} is the specific mesopore volume obtained from the BJH cumulative specific adsorption volume of pores of 1.70–300.00 nm in diameter.
[e] Average pore diameter is determined from the average of the BJH adsorption of pore diameters obtained in the adsorption branch of the N$_2$ isotherm.

of mesoporous structure. At the same time, the pore size distribution of the samples show (see the inset of Fig. 3) that both samples present a wide distribution of pore diameter located between 2.0 and 15.0 nm, and the pore size of the samples mainly distributes around 6.0 nm. This suggests that the incorporation of ferric oxides did not destroy the surface mesoporous structure of TNWs(B) support. Moreover, a bit decrease in the specific BET surface area was observed from 41.2 to 34.4 m^2 g^{-1} after decorated by ferric oxides, but almost not any changes were achieved in the case of pore volume (Table 1). The high BET surface area and porous structure of the Fe$_2$O$_3$/TNWs(B) provided better surface adsorption and mass transfer in the pore of the substrates.

To further ascertain the chemical nature and type of nanoparticles supported on the surface of TNWs(B), XPS measurement was carried out and the results are presented in Fig. 4. In the XPS spectra curve of Fe$_2$O$_3$/TNWs(B), the presence of Fe 2p3, Ti 2p3, and O 1s can be ascertained (Fig. 4a). As depicted in Fig. 4b, the binding energy of Fe 2p is observed at 711.0 and 724.7 eV, which is assigned to the spectra of Fe 2p1/2 and Fe 2p3/2 for the lattice Fe^{III}–O in Fe$_2$O$_3$, respectively [36]. In Fig. 4c, the Ti 2p3/2 and Ti 2p1/2 spin–orbital splitting photoemission spectra for Fe$_2$O$_3$/TNWs(B) are located at the binding energy of 458.0 and 463.9 eV, respectively. The

separation between these two peaks is 5.9 eV, which is in agreement with the XPS data of the previous literature [37]. However, it is obvious that small binding energy shift to higher energies can be observed compared to bare TNWs(B) (457.4 eV for Ti 2p3/2 and 463.2 eV for Ti 2p1/2), which indicates that the electron density of Ti 2p decreases with the loading of iron oxides. This shift can be ascribed to the formation of Ti–O–Fe bond in the crystal lattice and the electronegativity of Fe higher than Ti [38]. As shown in Fig. 4d, the spectrum of O1s can be resolved into two contributions for TNWs(B), the main band of O1s at 529.1 eV is assigned to the lattice oxygen (Ti–O–Ti), and the contribution at around 531.3 eV belongs to the surface hydroxyl groups (Ti–OH). After decorated with ferric oxides, the binding energy of the sample exhibits a broad peak around 530.2 eV, which can be fitted into three contributions: 529.3, 530.4, and 531.6 eV. The O1s peaks toward higher binding energy can be explained that the electron affinity of Fe$_2$O$_3$ is higher than TiO$_2$. The contributions of binding energy at 530.1 eV for Fe$_2$O$_3$/TNWs(B) corresponds to the lattice Fe–O of the Fe$_2$O$_3$ supported on the surface of TNWs(B) [39]. Moreover, an increase trend in the O 1s peak intensity at 531.6 eV can be noted in the case of the Fe$_2$O$_3$/TNWs(B), which reveals that more hydroxyl groups or chemisorbed water molecules were adsorbed on the surface of catalyst [40].
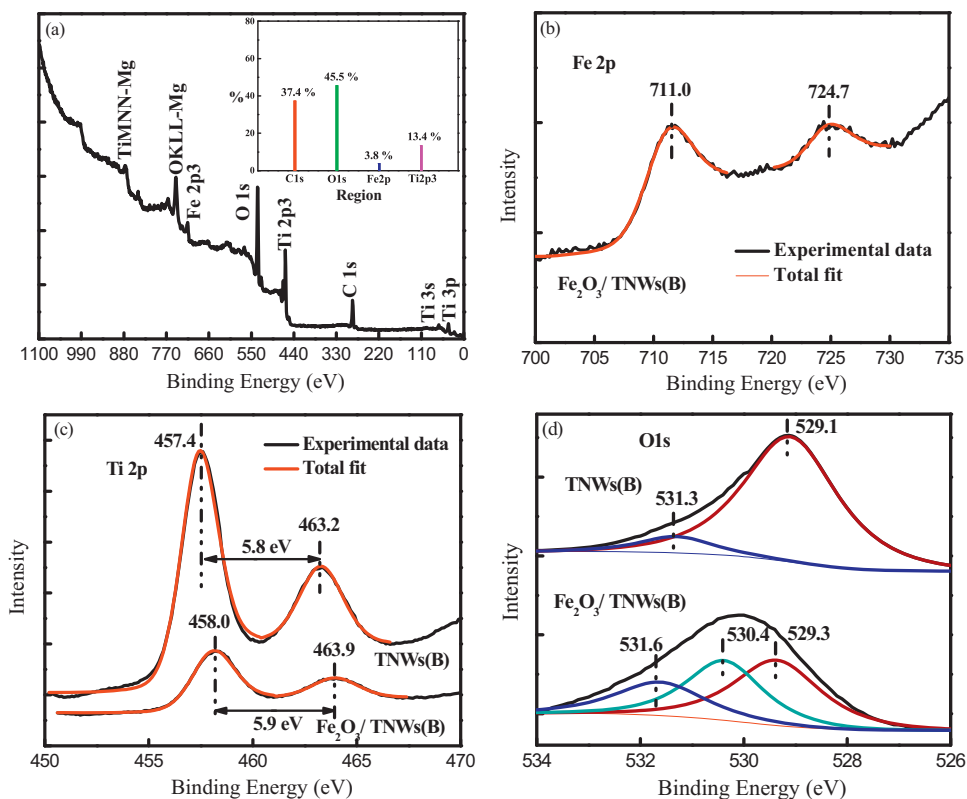
Fig. 4. XPS spectra of different samples: (a) full spectra of Fe$_2$O$_3$/TNWs(B), and fine spectra of (b) Fe 2p, (c) Ti 2P, (d) O 1s of pure TiO$_2$(B) nanowires and Fe$_2$O$_3$/TNWs(B).
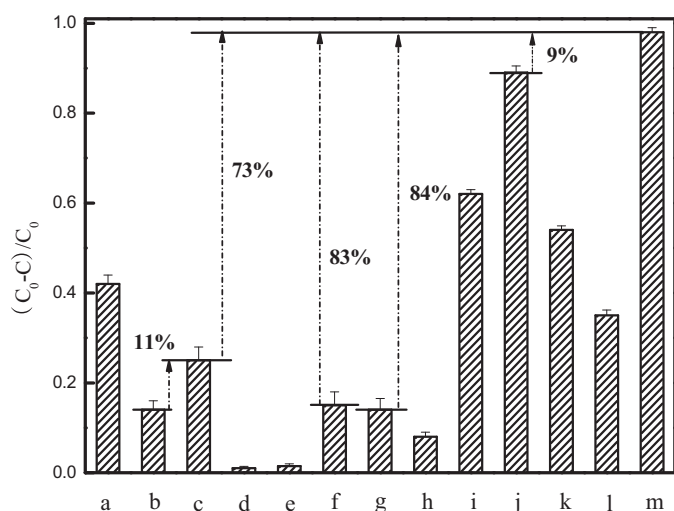
Fig. 5. Relative concentration of 4BS as a function of time at different procedure ($T = 298$ K, $C_{cat.} = 0.5$ g L^{-1}, $C_{4BS} = 100$ mg L^{-1}, $C_{H_2O_2,0} = 13.1$ mmol L^{-1}, pH$_0 = 6.5$): (a) P25–light; (b) TNWs(B)–light; (c) Fe$_2$O$_3$/TNWs(B)–light; (d) light–H$_2$O$_2$; (e) Fe$^{3\pm}$–light–H$_2$O$_2$; (f) Fe$_2$O$_3$–light–H$_2$O$_2$; (g) TNWs/(B)–light–H$_2$O$_2$; (h) Fe$_2$O$_3$/TNWs(B)–H$_2$O$_2$, (i) P25–light–H$_2$O$_2$; (j) Fe$_2$O$_3$/P25–light–H$_2$O$_2$; (k) Fe$_2$O$_3$/P25–light; (l) Fe$_2$O$_3$–TNWs(B)–light–H$_2$O$_2$, (m) Fe$_2$O$_3$/TNWs(B)–light–H$_2$O$_2$.

3.2. Photocatalytic activity of Fe2O3/TiO2(B) nanowires

The photocatalytic degradation of toxic and recalcitrant organic pollutants is of great importance in environmental protection and provides a commonly used way to characterize the activity of photocatalysts. Fig. 5 shows the efficiency of different catalytic oxidation for the degradation of dye 4BS. Besides the results of 4BS degradation by direct photolysis, it shows the results of photocatalytic test obtained using the synthesized TNWs(B), Fe$_2$O$_3$/TNWs(B) and Fe$_2$O$_3$/P25, as well as P25, Fe^{3+} ions and Fe$_2$O$_3$. The Fe$_2$O$_3$ particles were prepared by solvothermal method, and the concentration of Fe^{3+} was 1.0 mg L^{-1}, higher than the iron leaching during whole catalytic oxidation reaction. In the absence of H$_2$O$_2$, the degradation efficiency of Fe$_2$O$_3$/TNWs(B) was twice higher than that of bare TiO$_2$(B) nanowires under light irradiation, which indicated that the ferric oxides supported was of benefit to the TiO$_2$(B) nanowires photocatalytic activity enhanced. However, the best degradation efficiency of 4BS for Fe$_2$O$_3$/TNWs(B) was lower than 30%. In the case of P25 and P25 modified with iron oxides, the degradation efficiencies of dyes were above 40%, higher than that of Fe$_2$O$_3$/TNWs(B) and TNW(B). This indicates that the photocatalytic activity of prepared TiO$_2$(B) nanowires was lower than commercial P25 powders. In the presence of H$_2$O$_2$, 4BS was stable (0.5% photobleaching) without the catalysts under light irradiation, and underwent a slight degradation over Fe^{3+}, Fe$_2$O$_3$ particles and TNWs(B). Comparatively for sample Fe$_2$O$_3$/TNWs(B), the degradation efficiency of 4BS was greatly enhanced (98% photobleaching), much higher than that of the other catalysts. For samples P25 and Fe$_2$O$_3$/P25, the removal rates of dyes in photo-Fenton process were 62% and 89%, respectively, lower than that of Fe$_2$O$_3$/TNWs(B), which demonstrated that porous nanoarchitectures of TNWs(B) can not only enhance the loading and dispersion of Fe$_2$O$_3$ NPs on the supports, but also improve the contact between Fe$_2$O$_3$ and TiO$_2$ crystal planes. Moreover, the iron leaching of Fe$_2$O$_3$/P25 in Fenton oxidation reaction was about 1.5 mg L^{-1}, higher than that of sample Fe$_2$O$_3$/TNWs(B). This presents that Fe$_2$O$_3$/TNWs(B) exhibited an excellent ability and stability in the decomposition of H$_2$O$_2$ to hydroxyl radicals involved in the dye degradation under light irradiation. The photobleaching efficiency of dyes for sample TNWs(B) with the addition of synthesized Fe$_2$O$_3$ (4 wt% of TNWs(B)) was only

Table 2
Metal compositions in the prepared samples.

Sample	Metal content (wt%)	
	Fe	Ti
Fe$_2$O$_3$/TNWs(B)-0	1.97	47.71
Fe$_2$O$_3$/TNWs(B)-6	2.70	46.18
Fe$_2$O$_3$/TNWs(B)-12	2.73	50.53
Fe$_2$O$_3$/TNWs(B)-18	2.74	49.65

35%, much lower than that of TNWs(B) supporting with Fe$_2$O$_3$ NPs. In sharp contrast, it was found that the synergetic effect of Fe$_2$O$_3$ NPs supported and TNWs(B) was beneficial for enhancing the catalytic oxidation performance. However, without light irradiation, the photocatalytic activity of Fe$_2$O$_3$/TNWs(B) was as low as the Fe^{3+}, Fe$_2$O$_3$ and TNWs(B) catalysts. The performance enhancement induced by the light irradiation demonstrated that the activity of Fe$_2$O$_3$/TNWs(B) catalyst very intensely depended on the light, and irradiation should be an effective route to accelerate its rate-determining step. The effects of pH, catalyst loading and H$_2$O$_2$ dosage on catalytic activity of Fe$_2$O$_3$/TNWs(B) are presented in the supporting information (Figs. S1–3 in Supporting information (SI)).

3.3. Effect of size and location of the supported metal oxide NPs

The size and location of the metal oxide NPs and the interaction between metal NPs and their support had a significant effect on the catalytic properties and activity of the catalysts. In the present study, we attempted to control the size and location of Fe$_2$O$_3$ located on the surface of TNWs(B) by means of varying the impregnation duration time. By ICP analysis, the content of iron species for sample Fe$_2$O$_3$/TNWs(B)-0, Fe$_2$O$_3$/TNWs(B)-6, Fe$_2$O$_3$/TNWs(B)-12, and Fe$_2$O$_3$/TNWs(B)-18 was ca. 1.97, 2.70, 2.73 and 2.74 wt%, respectively (Table 2), which indicated that the impregnation time had a positive effect on enhancing the loading of iron oxides.

As schematically shown in Fig. 6, without impregnating before solvothermal process, more Fe^{3+} ions existed in solution were inclined to integrate with those ions stabilized at the interface of the support to form large NPs. The particle size of some aggregates was around 10.0 nm larger than that of TNWs(B) pores. When impregnating duration increased to 6 h (Fe$_2$O$_3$/TNWs(B)-6), the diameter of the nanocrystals loaded on the TNWs(B) surface decreased to less than 7.0 nm, and a few particles could disperse into the pores of the support. However, further increasing the impregnating time to 12 and 18 h (Fe$_2$O$_3$/TNWs(B)-12), the metal oxides nanoparticles disappeared from the external surface of TNWs(B) dramatically. We hypothesized that tiny ferric oxides formed were highly dispersed insider of the mesoporous network of TNWs(B) surface. This reveals that the long impregnation duration would further promote the migration of Fe^{3+} ions from the bulk into the surface of TNWs(B) support and provide steric restrictions to confine or prevent the growth of metal oxides NPs on the surface.

To further confirm our hypothesis, HRTEM analysis of the Fe$_2$O$_3$/TNWs(B)-12 was carried out, which reveals more detail concerning the crystal structure of the composite. Fig. 7a and b shows that most of the NPs were found to be much smaller than the pore size of the support, in which the size less than 2 nm appeared as insider of the mesopore, and the remaining NPs were uniformly immobilized on the matrix of TNWs(B). As shown in Fig. 7c, the confirmation that the nanowires should be TiO$_2$(B) was also obtained, the lattice spacing of 0.35 and 0.62 nm corresponds to (1 1 0) and (0 0 1) crystal planes of TiO$_2$(B), respectively. And the measured angle between the lattice planes is 107°, in good agreement with the theoretical value of monoclinic TiO$_2$(B). Importantly, it was clear that the highly crystallized nanoparticles were observed. We determined the interplanar distance of nanoparticles
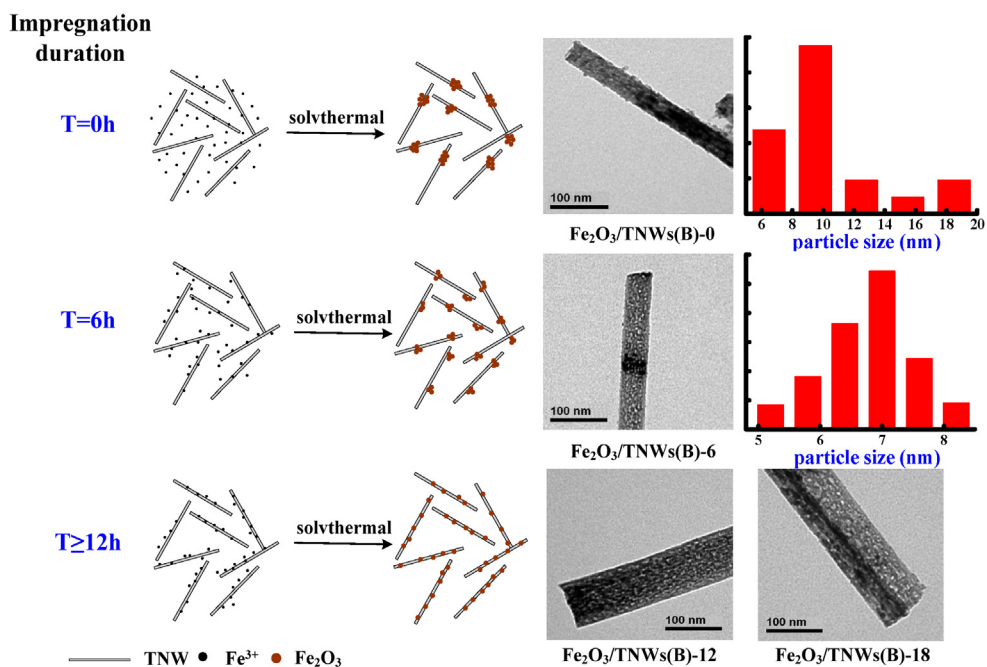
Fig. 6. Schematic diagram of different size and location of the Fe_2O_3 NPs supported on TNWs(B) via varying the impregnation duration time.
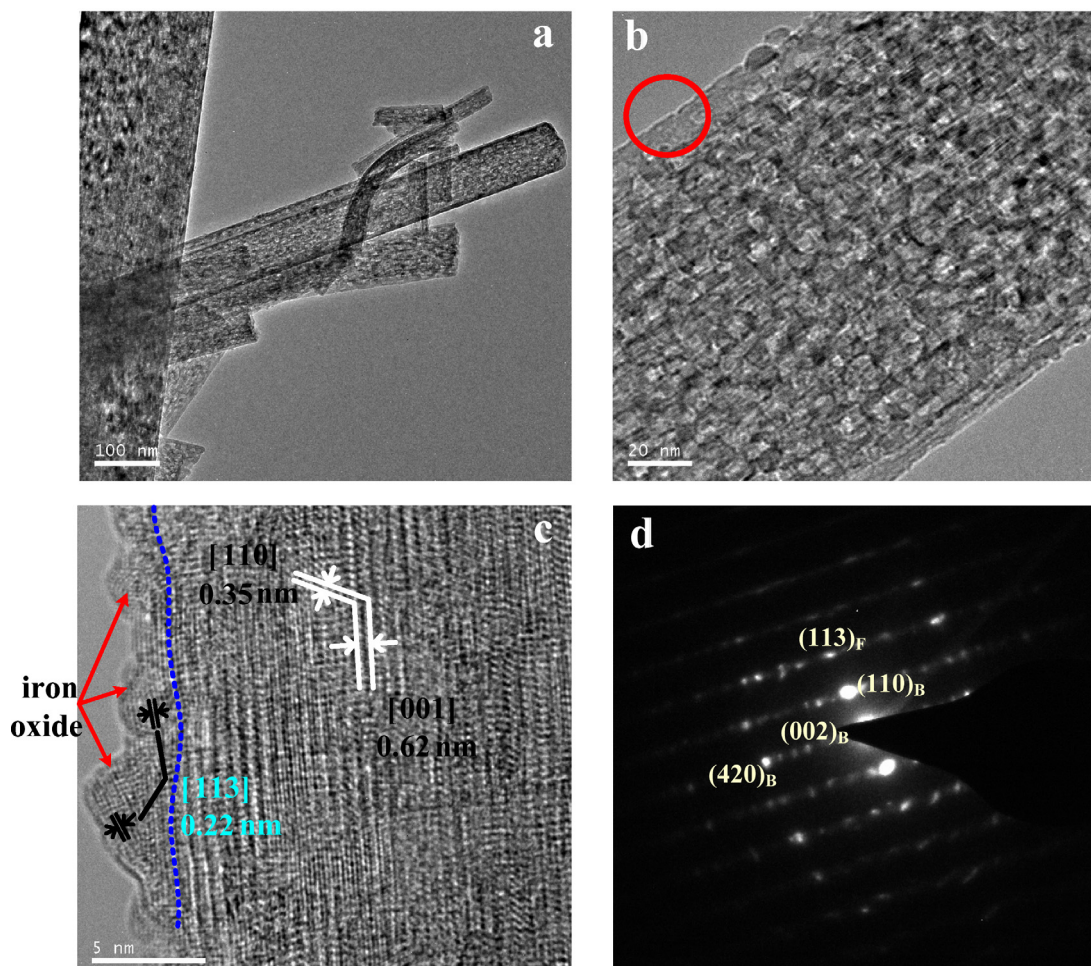

Fig. 7. TEM images and electron diffraction patterns of Fe_2O_3/TNWs(B)-12 (a–c), and selected area electron diffraction (SAED) pattern for corresponding sample (d).
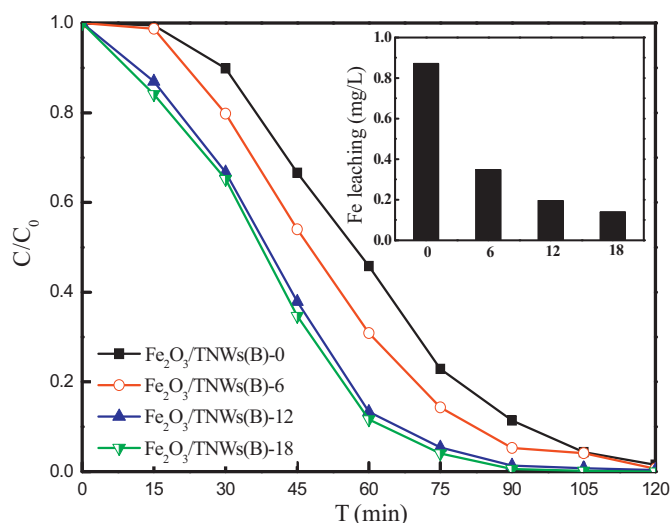
Fig. 8. Photo-Fenton decomposition of 4BS as function of time in the presence of catalysts prepared with different impregnation duration time. (T = 298 K, $C_{cat.}$ = 0.5 g L^{-1}, C_{4BS} = 100 mg L^{-1}, $C_{H_2O_2,0}$ = 13.1 mmol L^{-1}, pH$_0$ = 6.5).

Fig. 9. Reusability of the Fe$_2$O$_3$/TNWs(B)-12 catalyst after subsequent reactions (T = 298 K, $C_{cat.}$ = 0.5 g L^{-1}, C_{4BS} = 100 mg L^{-1}, $C_{H_2O_2,0}$ = 13.1 mmol L^{-1}, pH$_0$ = 6.5).

to be 0.22 nm, which corresponds well to the lattice spacing of the (1 1 3) planes of rhombohedral Fe$_2$O$_3$ structure (JCPDS 33-0664). As can be seen, (0 0 1) planes in TiO$_2$(B) and (1 1 3) planes of Fe$_2$O$_3$ matched perfectly to form a fixed interface, which are crucial to the charge separation and stability of the photocatalyst. The electron diffraction (ED) pattern of the sample further confirmed that the composites were composed of Fe$_2$O$_3$ and TiO$_2$(B) phases (Fig. 7d). The XRD and Raman analysis of Fe$_2$O$_3$/TNWs(B)-12 sample were also presented in supporting information (Fig. S4 in SI).

Fig. 8 shows catalytic performance of the composites with different size and location of the ferric oxide NPs supported. An obvious increase in degradation rate of 4BS was observed with the increase of impregnation duration time from 0 to 12 h. The observed low catalytic activity of the catalysts with less impregnation duration may be attributed to the large size of NPs and agglomeration on the surface of support, as confirmed by the TEM measurements. However, it was worthy to note that no significant enhancement on the degradation rate of dye was found when the impregnation duration time continued to be prolonged to 18 h, which exhibited that the extension of impregnation time had no effect on the particle size almost after attaining the adsorption equation. These observations provided a valuable insight for detailed understanding of the size- or location-dependent catalytic activity of catalysts. Combined with the TEM analysis, it showed that the photocatalytic activity of the samples decreased as the increase in particle size, and small metal oxides particles dispersed in pores of support (with d_{NPs} < 2 nm) were more active for catalytic reaction. It may be due to the fact that a large interface between the small and well dispersed NPs and the support, which facilitated the interfacial electron transfer between TiO$_2$(B) and Fe$_2$O$_3$. Moreover, in the whole catalytic oxidation process, the lost content of Fe ions on Fe$_2$O$_3$/TNWs(B)-0 was above 0.8 mg L^{-1}, much larger than that of Fe$_2$O$_3$/TNWs(B)-12 and Fe$_2$O$_3$/TNWs(B)-18. This reveals that the long impregnation time had a positive effect on the stability of Fe$_2$O$_3$ NPs on the support. Therefore, our results demonstrated that highly dispersed Fe$_2$O$_3$ nanoparticles in the well organized mesoporous frameworks were important for their activity and stability.

3.4. Catalyst stability

The reusability of the catalyst is the important factors for practical application. To confirm the possibility of recycle utilization
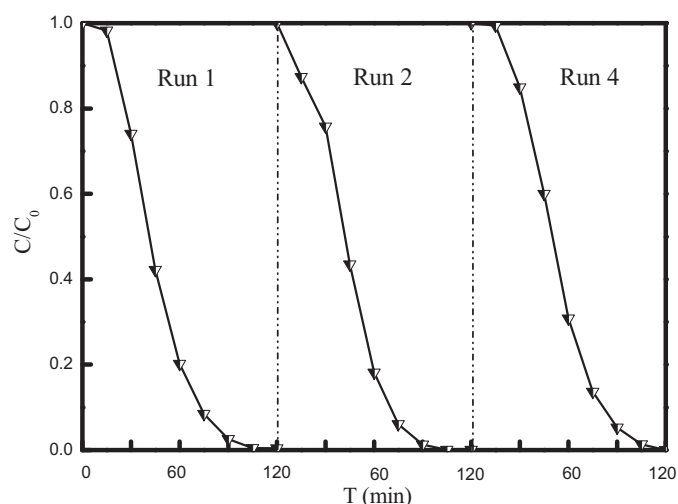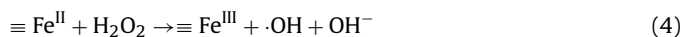
of the obtained catalyst, several cycles of the experiments are performed. Fig. 9 shows the durability of the Fe$_2$O$_3$/TNWs(B)-12 for 4BS degradation under light irradiation. The catalyst showed almost 100% repeatability for the four successive reused runs without any chemical regeneration in 120 min reaction time. The leaching of iron ions during the reaction process remained below 0.2 mg L^{-1} in all the cycles, which had insignificant influence on the catalytic performance (Fig. S5 in SI). The results clearly indicated that the Fe$_2$O$_3$/TNWs(B)-12 was stable and resistant to photo-corrosion during the photocatalytic reaction. This well demonstrated that mesoporous TNWs(B) provided a strong stabilization of small metal oxide nanoparticles (diameter <2 nm) highly dispersed in the surface porous matrix. Fig. 10 shows that TNWs(B) can be more easily separated by sedimentation from aqueous suspension less than 1 h after supporting by Fe$_2$O$_3$ NPs, while P25 still remained turbid. The observations presented that porous and fibrous nanoarchitecture loaded by nanoparticles can be easily separated from the reaction system simply by sedimentation, which was especially favorable for the long operation of heterogeneous catalysis on an industrial scale.

3.5. Synergistic effect of metal oxide NP and support on the photocatalytic performance

The experimental results above have clearly evidenced that the synergistic effect of metal oxides supported and TNWs(B) played a significant role in production of hydroxyl radicals under light irradiation. Here a tentative mechanism proposed for H$_2$O$_2$ decomposition is illustrated in Fig. 11a. To better clarify the mechanism, major possible reactions should be involved as follows (Eqs. (1)–(5)):

$$TiO_2 + h\nu \rightarrow h + e^- \tag{1}$$

$$h^+ + H_2O \rightarrow \cdot OH + H^+ \tag{2}$$

$$\equiv Fe^{III} + e^- \rightarrow \quad \equiv Fe^{II} \tag{3}$$

$$\equiv Fe^{II} + H_2O_2 \rightarrow \equiv Fe^{III} + \cdot OH + OH^- \tag{4}$$

$$^\bullet OH + 4BS \rightarrow \cdots \rightarrow CO_2 + H_2O \tag{5}$$

First, the porous structure of TiO$_2$(B) support could improve the light utilization efficiency, as some of the photons entered the porous structure and were absorbed by the TiO$_2$ and Fe$_2$O$_3$ NPs
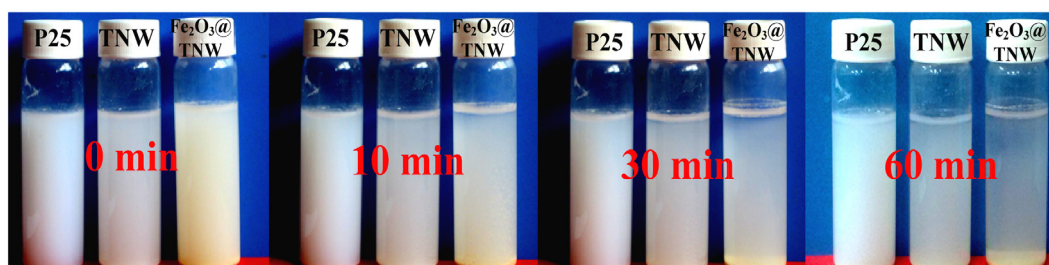
Fig. 10. Sedimentation for 1 h in aqueous suspensions of P25, TNWs(B) and Fe_2O_3/TNWs(B)-12 (pH = 6.8).

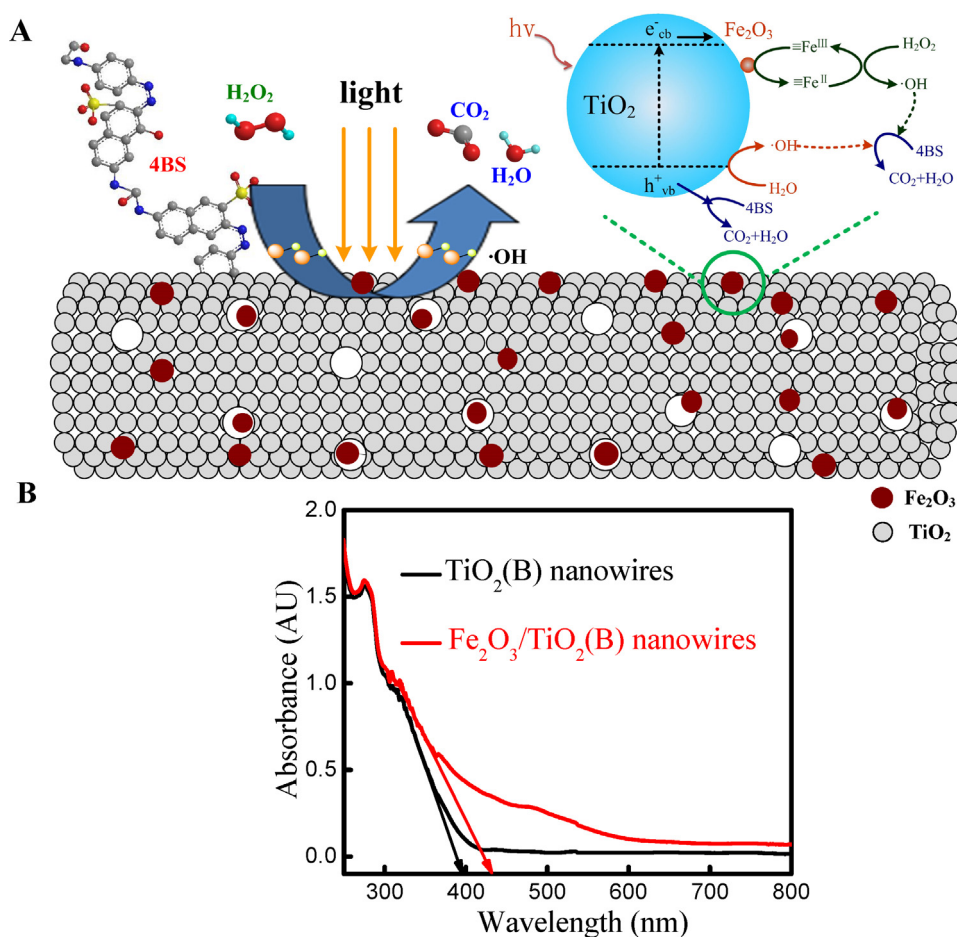**Fig. 11.** (A) Possible mechanism of heterostructure Fe_2O_3/TNWs(B) for degradation of 4BS under light irradiation; (B) UV−visible diffuse reflectance spectra of pure TNWs(B) and Fe_2O_3/TNWs(B).

[41,42]. At the same time, the well-matched phase interfaces of heterostructure of TiO_2(B) and Fe_2O_3 NPs promoted the separation of photo-induced electrons and holes and suppressed charge recombination. Since the conduction band (CB) of Fe_2O_3 laid more positive than that of TiO_2(B), Fe_2O_3 loaded on the surface of TiO_2(B) nanowires made it possible for the photogenerated electrons to migrate from TiO_2(B) to Fe^{III} and further converted to Fe^{II}. As reported, Fe^{II} has a big potential for decompostion of H_2O_2 to ·OH radicals in organic pollutant degradation [43]. On the other hand, the photogenerated holes accumulated in the valence band (VB) of TiO_2 could be favorable for the transformation of H_2O to hydroxyl radicals. Clearly, metal oxides supported accelerated efficient charge transfer in the composite material, and consequently efficiently enhanced the photocatalytic activity.

Moreover, the heterostructure of Fe_2O_3/TNWs(B) had a wider range of light absorption. Fig. 11b shows the UV−visible diffuse

reflectance spectra (DRS) of the samples. As apparent from figure, the loading of metal oxides promoted the light harvesting ability and further extended the absorption range, as compared with highly porous TNWs(B). As reported before, TiO_2(B) is an n-type semiconductor with a band gap of 3–3.22 eV [44]. In the present study, after supporting by Fe_2O_3 NPs, the absorption edge of TNWs(B) shifted from 395 (ca. 3.19 eV) to 433 nm (ca. 2.94 eV) due to the narrow band gap of Fe_2O_3 (ca. 2.06 eV) [45]. Therefore, the enhanced absorption range of light for Fe_2O_3/TNWs(B) composite can play an important role in the photocatalysis.

4. Conclusions

In summary, we have presented a simple but effective approach to immobilize Fe_2O_3 NPs on the mesoporous TiO_2(B) nanowires in one step. Such fibrous and heterostructured material thus

introduces a new type of photocatalyst, which not only can greatly promote H_2O_2 to generate highly aggressive hydroxyl radicals for the organic pollutants degradation, but also be easily separated from the reaction medium and maintain its high activity. The impregnation duration had significant effect on size and location of NPs supported on TNWs(B). By analysis, it is concluded that the high and stable photocatalytic performance of Fe_2O_3/TNWs(B) can be attributed to the high dispersion of tiny nanoparticles in the mesoporous frameworks of TiO_2(B) nanowires and the efficient charge transfer in the fixed interfaces between two phases. The synergetic effect of Fe_2O_3 NPs and TNWs(B) support played an important role in photochemical oxidation reaction. The progresses presented here not only produce a novel heterostructure Fe_2O_3/TNWs(B), but also provides a valuable insights for detailed understanding of the structure-dependent photochemical activity of catalysts.

Acknowledgments

Appendix A. Supplementary data

Supplementary data associated with this article can be found, in the online version, at http://dx.doi.org/10.1016/j.apcatb.2013.12.055.

References

[1] A. Fujishima, K. Honda, Nature 238 (1972) 37.
[2] D.V. Bavykin, A.A. Lapkin, P.K. Plucinski, J.M. Friedrich, F.C. Walsh, J. Catal. 235 (2005) 10.
[3] X. Chen, S.S. Mao, Chem. Rev. 107 (2007) 2891.
[4] J.H. Park, S. Kim, A.J. Bard, Nano Lett. 6 (2006) 24.
[5] S.K. Mohapatra, M. Misra, V.K. Mahajan, K.S. Raja, J. Catal. 246 (2007) 362–369.
[6] R. Marchiand, L. Brohan, M. Tournoux, Mater. Res. Bull. 15 (1980) 1129.
[7] X.W. Wang, X.P. Gao, G.R. Li, L. Gao, T.Y. Yan, Appl. Phys. Lett. 91 (2007) 143102.
[8] O.K. Varghese, D. Gong, M. Paulose, K.G. Ong, E.C. Dickey, C.A. Grimes, Adv. Mater. 15 (2003) 624.
[9] M. Adachi, Y. Murata, J. Takao, J. Jiu, N. Sakamoto, F. Wang, J. Am. Chem. Soc. 126 (2004) 14943.
[10] A.R. Armstrong, G. Armstrong, J. Canales, P.G. Bruce, Angew. Chem. Int. Ed. 43 (2004) 2286.
[11] A.R. Armstrong, J. Canales, R. Garcia, P.G. Bruce, Adv. Mater. 17 (2005) 862.
[12] Y. Ren, Z. Liu, F. Pourpoint, A.R. Armstrong, C.P. Grey, P.G. Bruce, Angew. Chem. Int. Ed. 51 (2012) 2164.
[13] K. Pan, Y. Dong, C. Tian, W. Zhou, G. Tian, B. Zhao, H. Fu, Electrochim. Acta 54 (2009) 7350.
[14] A.K. Chakraborty, Z. Qi, S.Y. Chai, C. Lee, S.Y. Park, D.J. Jang, W.I. Lee, Appl. Catal., B 93 (2010) 368.
[15] D.R. Rolison, Science 299 (2003) 1698.
[16] W. Li, Y. Bai, C. Liu, Z. Yang, X. Feng, X. Lu, N.K.V. DerLaak, K.Y. Chan, Environ. Sci. Technol. 43 (2009) 5423.
[17] W. Li, C. Liu, Y. Zhou, Y. Bai, X. Feng, Z. Yang, L. Lu, X. Lu, K.Y. Chan, J. Phys. Chem. C 112 (2008) 20539.
[18] D. Yang, H. Liu, Z. Zheng, Y. Yuan, J. Zhao, E.R. Waclawik, X. Ke, H. Zhu, J. Am. Chem. Soc. 131 (2009) 17885.
[19] B. Liu, A. Khare, E.S. Aydil, ACS Appl. Mater. Interfaces 3 (2011) 4444.
[20] J. Thomas, M. Yoon, Appl. Catal., B 502 (2012) 111–112.
[21] Y. Bai, W. Li, C. Liu, Z. Yang, X. Feng, X. Lu, K.Y. Chan, J. Mater. Chem. 19 (2009) 7055.
[22] A. Naldoni, M. D'Arienzo, M. Altomare, M. Marelli, R. Scotti, F. Morazzoni, E. Selli, V.D. Santo, Appl. Catal., B 239 (2013) 130–131.
[23] N. Farhangi, R.R. Chowdhury, Y. Medina-Gonzalez, M.B. Ray, P.A. Charpentier, Appl. Catal., B 110 (2011) 25.
[24] C.H. Lin, J.H. Chao, C.H. Liu, J.C. Chang, F.C. Wang, Langmuir 24 (2008) 9907.
[25] A. Ghicov, P. Schmuki, Chem. Commun. (2009) 2791.
[26] S.K. Mohapatra, S. Banerjee, M. Misra, Nanotechnology 19 (2008) 315601.
[27] A.I. Kontos, V. Likodimos, T. Stergiopoulos, D.S. Tsoukleris, P. Falaras, I. Rabias, G. Papavassiliou, D. Kim, J. Kunze, P. Schmuki, Chem. Mater. 21 (2009) 662.
[28] Z.H. Xu, J.G. Yu, Nanoscale 3 (2011) 3138.
[29] L.F. Cui, F. Huang, M.T. Niu, L.W. Zeng, J. Xu, Y.S. Wang, J. Mol. Catal. A 326 (2010) 1.
[30] Y. Yu, D. Xu, Appl. Catal., B 73 (2007) 166.
[31] X.W. Zhang, T. Zhang, J.W. Ng, D.D. Sun, Adv. Funct. Mater. 19 (2009) 3731.
[32] L.W. Zhu, L. Gu, Y. Zhou, S.L. Cao, X.B. Cao, J. Mater. Chem. 21 (2011) 12503.
[33] X.W. Zhang, J.H. Pan, A.J. Du, J.W. Ng, D.D. Sun, J.O. Leckie, Mater. Res. Bull. 44 (2009) 1070.
[34] Y. Yalçın, M. Kılıç, Z. Çınar, Appl. Catal., B 99 (2010) 469.
[35] J.F. Zhu, J.L. Zhang, F. Chen, M. Anpo, Mater. Lett. 59 (2005) 3378.
[36] C.D. Wagner, W.M. Riggs, L.E. Davis, J.F. Moulder, G.E. Muilenberg, Handbook of X-ray Photoelectron Spectroscopy, Perkin-Elmer Corporation, Physical Electronics Division, USA, 1979.
[37] N. Ohtsu, N. Masahashi, Y. Mizukoshi, K. Wagatsuma, Langmuir 25 (2009) 11586.
[38] O. Akhavan, R. Azimirad, Appl. Catal., A 369 (2009) 77.
[39] L. Armelao, R. Bertoncello, L. Crociani, J. Mater. Chem. 5 (1995) 79.
[40] Y.Q. Liang, Z.D. Cui, S.L. Zhu, Y. Liu, X.J. Yang, J. Catal. 278 (2011) 276.
[41] B. Lu, C. Zhu, Z. Zhang, W. Lan, E. Xie, J. Mater. Chem. 22 (2012) 1375.
[42] C. Zhu, B. Lu, Q. Su, E. Xie, W. Lan, Nanoscale 4 (2012) 3060.
[43] M.A. Fontecha-Cámaraa, M.A. Álvarez-Merinoa, F. Carrasco-Marínb, M.V. López-Ramóna, C. Moreno-Castillab, Appl. Catal., B 101 (2011) 425.
[44] S. Ahmed, S.M. Fonseca, T.J. Kemp, P.R. Unwin, J. Phys. Chem. B 107 (2003) 5892.
[45] T.K. Townsend, E.M. Sabio, N.D. Browning, F.E. Osterloh, Energy Environ. Sci. 4 (2011) 4270.